Geomechanics and Engineering, *Vol. 29, No. 5 (2022) 567-582*
https://doi.org/10.12989/gae.2022.29.5.567

Study on failure behaviors of mixed-mode cracks under static and dynamic loads

Lei Zhou[1,2,3], Jianxing Chen[3], Changlin Zhou[4], Zheming Zhu[*3], Yuqing Dong[**3] and Hanbing Wang[3]

[1]*Shock and Vibration of Engineering Materials and Structures Key Laboratory of Sichuan Province, Southwest University of Science and Technology, Mianyang 621010, Sichuan, China*
[2]*Key Laboratory of Deep Earth Science and Engineering (Ministry of Education), College of Architecture and Environment, Sichuan University, Chengdu 610065, China*
[3]*Failure Mechanics & Engineering Disaster Prevention and Mitigation, Key Laboratory of Sichuan Province, College of Architecture and Environment, Sichuan University, Chengdu 610065, China*
[4]*Chengdu Surveying Geotechnical Research Institute Co., Ltd. of MCC, Chengdu, 610023, China*

(Received April 19, 2021, Revised April 17, 2022, Accepted April 27, 2022)

Abstract. In the present study, a series of physical experiments and numerical simulations were conducted to investigate the effects of mode I and mixed-mode I/II cracks on the fracture modes and stability of roadway tunnel models. The experiments and simulations incorporated different inclination angle flaws under both static and dynamic loads. The quasi-static and dynamic testing were conducted by using an electro-hydraulic servo control device and drop weight impact system (DWIS), and the failure process was simulated by using rock failure process analysis (RFPA) and AUTODYN software. The stress intensity factor was also calculated to evaluate the stability of the flawed roadway tunnel models by using ABAQUS software. According to comparisons between the test and numerical results, it is observed that for flawed roadways with a single radical crack and inclination angle of 45°, the static and dynamic stability are the lowest relative to other angles of fractured rock masses. For mixed-mode I/II cracks in flawed roadway tunnel models under dynamic loading, a wing crack is produced and the pre-existing cracks increase the stress concentration factor in the right part of the specimen, but this factor will not be larger than the maximum principal stress region in the roadway tunnel models. Additionally, damage to the sidewalls will be involved in the flawed roadway tunnel models under static loads.

Keywords: dynamic loads; failure behavior; flawed roadway tunnel models; mixed-mode crack; static loads

1. Introduction

During mineral resource excavation by blasting or shock waves, many radial flaws may be produced in the surrounding rock mass; these may be caused by different fracture modes under dynamic or static loads, such as those arising from overburden pressures, in situ stresses, and earthquake waves (Fan *et al.* 2019, Haeri *et al.* 2014, Wu *et al.* 2019, 2020). As these flaws are subjected to various load conditions in practical working conditions, they may initiate, propagate, and coalesce along different directions; they may also weaken the rock mass strength, ultimately leading to various geologic hazards (Sarfarazi *et al.* 2017, Yu *et al.* 2020). Therefore, the flaws in a real roadway may greatly influence the roadway stability, and a corresponding study on mixed-mode crack failure behaviors under dynamic loads is of great importance. In this study, the influences of static and impact loads on the failure properties and stability of flawed roadway tunnel models are studied.

Underground chamber projects are generally subjected to various loading conditions in their real geological environments. Owing to the arbitrary orientation of cracks relative to the loading orientations, research is required on the failure resistance of cracked rock masses subjected to static or dynamic loads. The failure behaviors and processes of mixed-mode I/II cracks have attracted increasing attention, owing to their significance in regards to the security and stability of underground projects in practical engineering problems. Many research achievements have been studied in theoretical and experimental analyses of mixed-mode fractures under complex loading conditions (Alneasan *et al.* 2019, Li *et al.* 2019b, Rege *et al.* 2019). Lesiuk *et al*. (2020) conducted mixed-mode (I/II) tests to acquire fatigue crack propagation trajectories for typical rail steel by using compact tension shear specimens. Aliha, *et al*. (2016) used four polymethyl methacrylate samples with different test dimensions and different crack types to investigate initiation directions and initiation toughness under static loads. Xu and Li (2012) utilized a split Hopkinson tension bar (SHTB) device and finite element method to measure dynamic mixed-mode fracture initiation toughness values of materials under impact loading. Wang *et al*. (2011) studied the variations in the dynamic initiation toughness values of mode I and mode II cracks with the size of specimen using an SHPB device, and indicated that the trend for mode II cracks was more remarkable than that for mode I cracks. Wang *et al*. (2017) investigated the initiation

*Corresponding author, Ph.D.
E-mail: zhemingzhu@hotmail.com
**Corresponding author, Ph.D.
E-mail: dong03@foxmail.com

ISSN: 2005-307X (Print), 2092-6219 (Online)

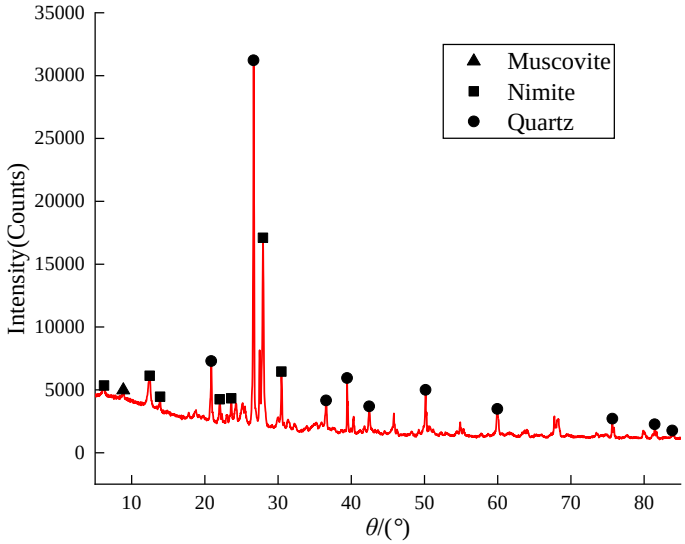

Fig. 1 Results of XRD analysis

and propagation characteristics of mixed-mode cracks under impact loads and proposed a single cleavage semicircle compression sample for determining crack fracture toughness. Through the above research results, a solid foundation has been established for clarifying the failure mechanisms of mode I and mixed-mode I/II cracks (Ajdani *et al.* 2020, Aliha and Ayatollahi 2014). However, these studies did not consider the influence of cracks on the stability of rock structures or tunnel engineering; this is a non-ignorable external factor, as it can induce rock mass instability. In so far as mixed-mode cracks in real tunnel engineering under dynamic loads, the research results have difficulty meeting the engineering needs.

Numerical simulations have been widely implemented to analyze the failure mechanisms of deep underground structures under static or dynamic loads. The popular numerical algorithms for rock fracture simulations can be strictly grouped into two categories: continuum-based approach and discrete element approach. Finite element method (FEM) (Xie *et al.* 2019) and finite difference method (FDM) (Wang *et al.* 2021, Zhou *et al.* 2020, 2018b) are typical continuum-based methods and widely used in the field of fracture mechanics. Jia and Tang (2008) applied FEM-based rock failure process analysis (RFPA) software to investigate the effects of various slopes of lateral pressure coefficients and layered joints on the failure behaviors of roadways. Hadi and Sarfarazi (Haeri *et al.* 2020, 2018, Sarfarazi *et al.* 2018) used FEM-based ABAQUS software to investigate the impact of the joint number and its angularities on the fracture modes of a joint bridge area and its tensile strength. Li *et al*. (2018) used FDM-based software AUTODYN to analyze the influence of a blasting hole in a tunnel on the crack propagation behaviors under blasting loads. Du *et al*. (2020) used FDM-based "Fast Lagrangian Analysis of Continua in 3 Dimensions" software to study the stability and fracture properties of a roadway.

Discrete element method (DEM) (Mitra *et al.* 2015) and discontinuous deformation analysis (DDA) (Shi 1992) method are typical discrete element approach, which are used to solve the problems of large deformation and discontinuity. Some numerical algorithms, such as extended FEM (XFEM) and boundary element method (BEM), are equivalent continuum based on classical theory. Discontinuous deformation and displacement analysis (DDD) proposed by Tang *et al*. (2015) combines DDA and FEM methods and have the advantages in characterizing the complete failure process.

Hence, in this study, to better understand the failure behaviors of mixed-mode cracks in the surrounding rock of a roadway under dynamic and static loads, a series of static and dynamic laboratory experiments were conducted by employing flawed roadway tunnel models with different inclination angle flaws. An electro-hydraulic servo press and drop weight test machine were adopted as testing tools, both of which having been applied in the past for various static experiments and impact experiments (Huang *et al.* 2019, Reddish *et al.* 2005). In addition, RFPA and AUTODYN software were implemented to simulate the failure characteristics of the flawed roadway samples, and their stability was estimated under different loading conditions (Huang *et al.* 2017, Zuo *et al.* 2015).

2. Flawed roadway tunnel model tests

2.1 Rock material

The raw material applied in this research was a green sandstone widely available in the Sichuan Province of China. It can be regarded as isotropic and homogeneous, and has been studied by many scholars in recent years (Ying *et al.* 2020, Zhou *et al.* 2019). The microscopic experiments were carried out utilizing X-ray diffraction (XRD) analysis and scanning electron microscopy (SEM), as illustrated in Figs. 1 and 2, respectively. The mineral components of the green sandstone were mainly quartz, nimite, and muscovite with the grain sizes between 0.005 and 0.2, 0.08 to 0.2, and 0.03 to 0.06 mm. The physical and mechanical properties of green sandstone were presented in Table 1.

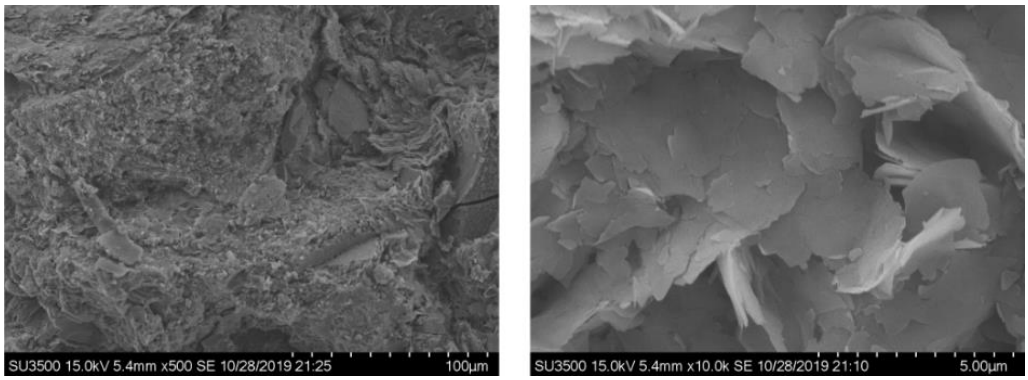

Fig. 2 Results of SEM analysis

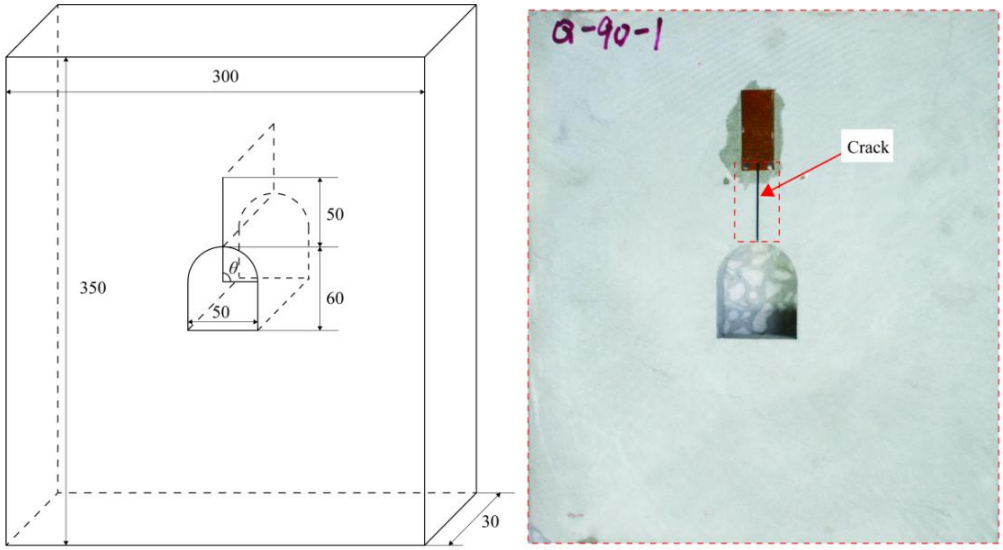

Fig. 3 Sketch map and photograph view of the flawed roadway sample (unit: mm)

Table 1 Physical and mechanical properties of green sandstone

Properties	Value
Density (kg/m^3)	2215
Uniaxial compression strength (MPa)	22.08
Brazilian tensile strength (MPa)	3.53
Mode I fracture initiation toughness (MPa·m$^{1/2}$)	0.31
Elastic modulus(MPa)	13.57
Poisson's ratio	0.165
Longitudinal wave velocity(m/s)	2684
Shear wave velocity(m/s)	1689
Rayleigh wave velocity(m/s)	1457

2.2 Test method and sample manufacturing

A sketch map and photograph view of the flawed roadway tunnel model are illustrated in Fig. 3. In the present study, horseshoe configuration roadway tunnel model experiments were conducted, and a single radial flaw was considered around the edge of the horseshoe roadway.

A radical flaw (50 mm) was set at the roadway roof, and a total of seven groups of samples were prepared, with different inclination angles θ (from 0° to 90°, with a 15° gradient increment) between the flaw and horizontal axis. The flawed roadway tunnel models were square plates measuring 350 mm × 300 mm × 30 mm. The horseshoe roadway (60 mm × 50 mm) was placed in the center of the roadway tunnel model, and the arch of the roadway comprised a semi-circle with an arch diameter of 50 mm. Subsequently, 70–100 samples were fabricated for quasi-static fracture experiments and dynamic fracture experiments, thereby ensuring that at least three effective data sets were obtained for each group. During fabrication, all surfaces of the samples were carefully ground and polished to ensure an unevenness and non-perpendicularity of less than 0.10 mm. Meanwhile, the cracks were first punched by high-pressure water jets, and then the crack tips were sharpened with a 0.2 mm hacksaw blade, and the radius of the crack tip was approximately 0.1 mm.

2.3 Quasi-static fracture experiments

Conventional compression experiments were conducted at a constant displacement speed of 0.1 mm/min by using an electro-hydraulic servo control device (500 T), as shown in

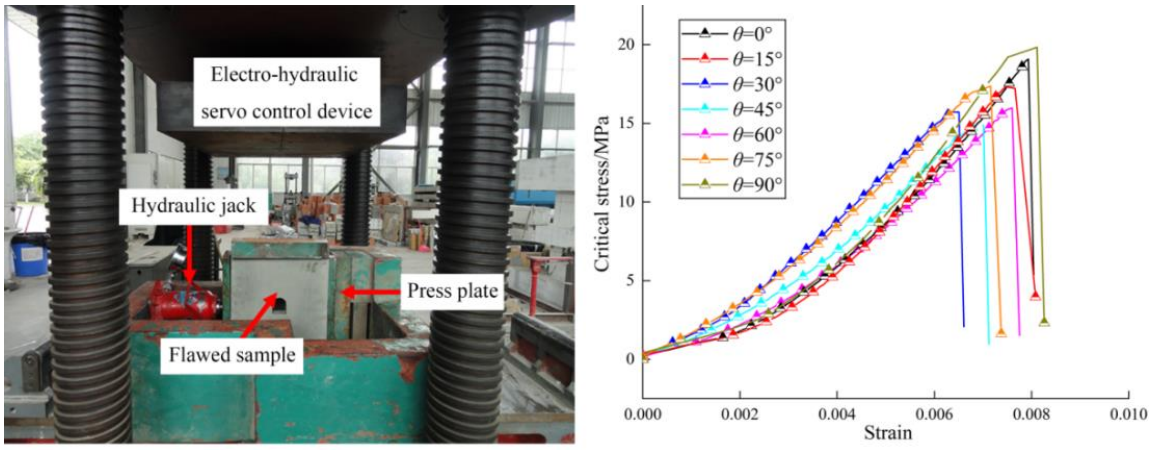

(a) Quasi-static fracture experiments test system (b) Stress-strain plots recorded by computer

Fig. 4 Quasi-static fracture experiments test system and test results

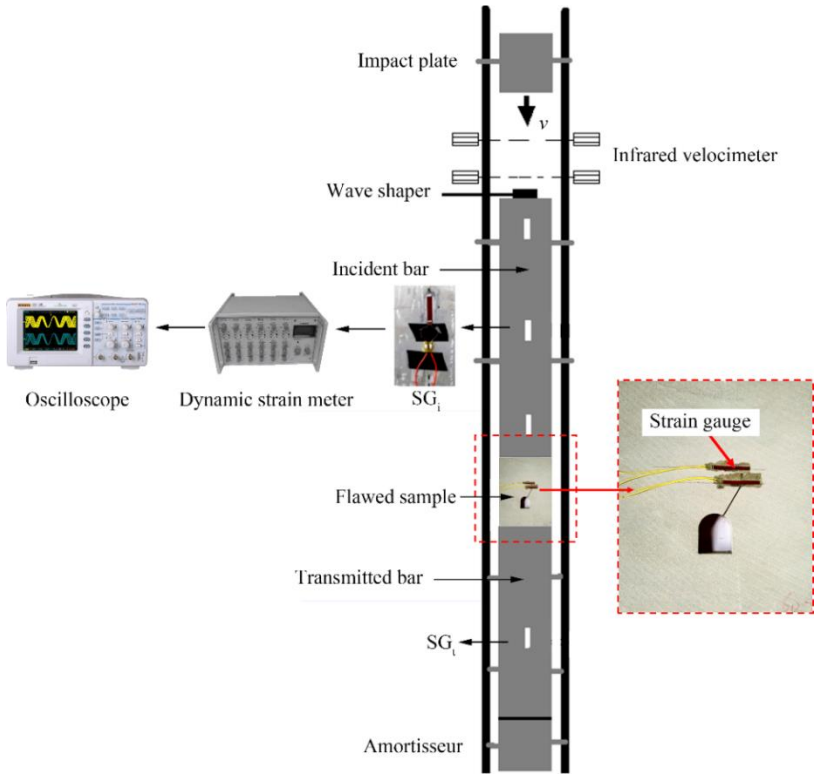

Fig. 5 Drop weight impact system (DWIS)

Fig. 4(a). To consider the effect of the lateral pressure on a real roadway structure, a confining pressure was applied to both sides of the roadway tunnel models utilizing two steel plates; this allowed the entire roadway tunnel model to maintain a state of biaxial compression. One steel plate was loaded by a hydraulic jack with a pressure gauge (such that the pressure value could be revealed accurately), and the other side was fixed. Before testing, 2.5 MPa pressure was loaded by the hydraulic jack, and the vertical stress was loaded through the electro-hydraulic servo control device until the entire flawed roadway tunnel model failed. During testing, a computer automatically collected plots of the stress, strain, displacement, and pressure versus time, as shown in Fig. 4(b). From the stress–strain curves for the samples with a flaw inclination angle θ from 0° to 90°, it can be observed that the failure peak stresses of the flawed samples with various inclination angles θ were quite different.

2.4 Dynamic fracture experiments

The impact compression experiments were carried out by using a drop weight impact system (DWIS) comprising a striker (150 mm × 300 mm × 30 mm), incident plate (3000 mm × 300 mm × 30 mm), transmitted plate (200 mm × 300 mm × 30 mm), amortisseur, and data acquisition system, as illustrated in Fig. 5. The longitudinal wave velocity, density, elastic modulus, and Poisson's ratio of the three plates were

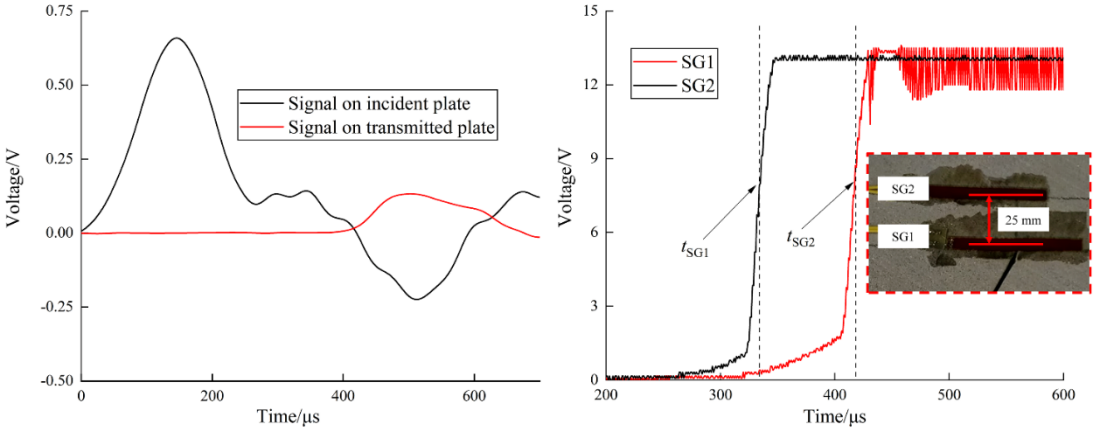

(a) Electrical signals collected using strain gauges (b) Dynamic fracture initiation time

Fig. 6 Electrical signals collected using strain gauges and dynamic fracture initiation time collected using strain gauges

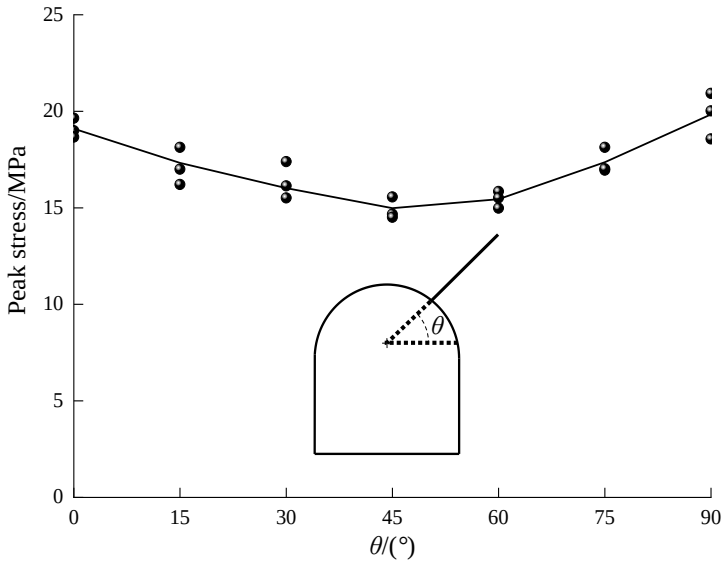

Fig. 7 Testing results of peak stress.

5006.5 m/s, 1, 2850 kg/m^3, 71.7 GPa, and 0.3, respectively.

During testing, the flawed roadway tunnel models were placed between the incident and transmitted plates, with butter applied on the surfaces of the sample and plates. The strike of the striker on the top of the incident plate produced a slowly rising half-sine stress impulse. As the compressive impulse (incident impulse) reached the plate-sample interface, a portion was reflected into the incident plate (reflected impulse), and the other portion was transmitted through the sample and then entered the transmitted plate (transmitted impulse). The three impulses were recorded (as shown in Fig. 6(a)) by utilizing strain gauges glued on the plates, and were defined as the incident strain impulse $\varepsilon_i(t)$, reflected strain impulse $\varepsilon_r(t)$, and transmitted strain impulse $\varepsilon_t(t)$, respectively. According to the one-impulse propagation theory, the impact loads could be acquired as follows (Li *et al.* 2019a)

$$\sigma_i(t) = E(\varepsilon_i(t) + \varepsilon_r(t)) \tag{1}$$

$$\sigma_t(t) = E\varepsilon_t(t) \tag{2}$$

To test the dynamic initiation time and average speed of crack propagation, two strain gauges (SG1 and SG2) were glued at the crack tip at a distance of 25 mm along the crack trajectories and perpendicular to the flaw, as illustrated in Fig. 6(b). As shown, SG1 at $\theta = 45°$ (No. 1) was cut at 334 μs, and SG2 was cut at 416 μs; in line with the fracture time of the strain gauges, the dynamic fracture initiation time and average speed of crack propagation in all of the flawed roadway tunnel models could be measured during testing.

2.5 Experimental results

2.5.1 Quasi-static fracture experimental results

As shown in Fig. 7, the failure stresses of the flawed roadway tunnel models with different inclination angles θ change remarkably. As $\theta = 45°$, the average peak stress is at the minimum in all groups, and is only 14.98 MPa for the

Table 2 Comparisons between experimental and simulation results under static loads

θ	Peak stress/MPa (average experimental results)	Peak stress/MPa (simulation results)	Error/%
No flaw	22.08	19.80	10.32
0°	19.10	19.18	0.42
15°	17.33	18.26	5.37
30°	16.02	17.25	7.68
45°	14.98	16.24	8.41
60°	15.45	18.09	17.08
75°	17.37	19.08	9.84
90°	19.84	19.23	3.07

Table 3 Comparisons between experimental and simulation results under dynamic loads

θ^*	Dynamic initiation time/μs (average experimental results)	Dynamic initiation time/μs (simulation results)	Error/%	Dynamic initiation toughness/ MPa·m$^{1/2}$	
				K_I^d	K_{II}^d
30°	385.00	377.73	1.89	-5.81	-3.73
45°	342.33	356.16	4.04	-3.76	-3.92
60°	362.33	364.75	0.67	-1.71	-2.74
75°	441.67	399.53	9.54	-0.38	-2.68
90°	518.33	465.61	10.17	0.84	0

*θ: At θ = 0° and 15°, a crack does not initiate in the experimental results

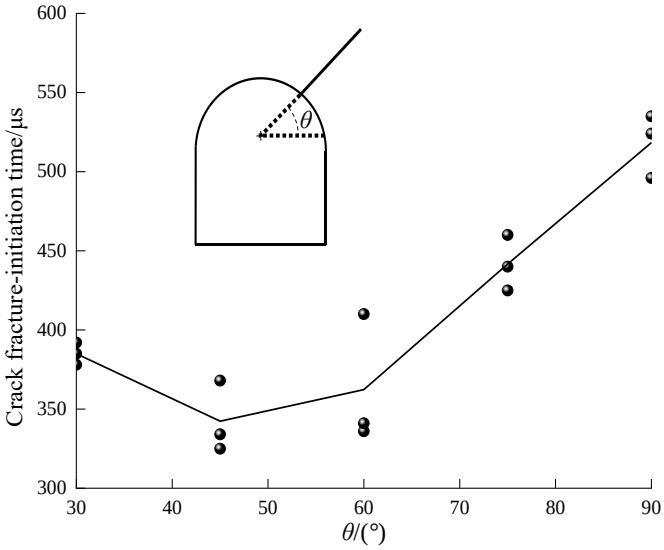

Fig. 8 Crack fracture-initiation time measured by strain gauges

sandstone model. This indicates that the radical flaw in this condition is the most unfavorable for roadway stability. All test results regarding the failure stress were listed in Table 2. It can also be observed that the failure stress of the flawed roadway tunnel models initially decreases with the inclination angle θ, and then increases. In addition, the static strength of each group is lower for the flawed sample than for the intact sample.

2.5.2 Dynamic fracture experimental results

In line with the dynamic crack initiation times as measured by SG1 and SG2, one can find that the dynamic initiation time changes significantly with the crack inclination angle θ under the impact loads, as illustrated in Fig. 8. At θ = 0° and θ = 15°, the crack is not initiated, and the dynamic initiation times cannot be acquired by SG1 and SG2. From the test results, it can be seen that at θ = 45°, the dynamic initiation time is the smallest, indicating that the dynamic stability of this roadway tunnel model is the lowest. For θ = 90°, the dynamic initiation time is the largest, implying that the mixed-mode I/II crack is easier to initiate than a pure mode I crack under dynamic loads. All of test results regarding the dynamic fracture initiation time were presented in Table 3.

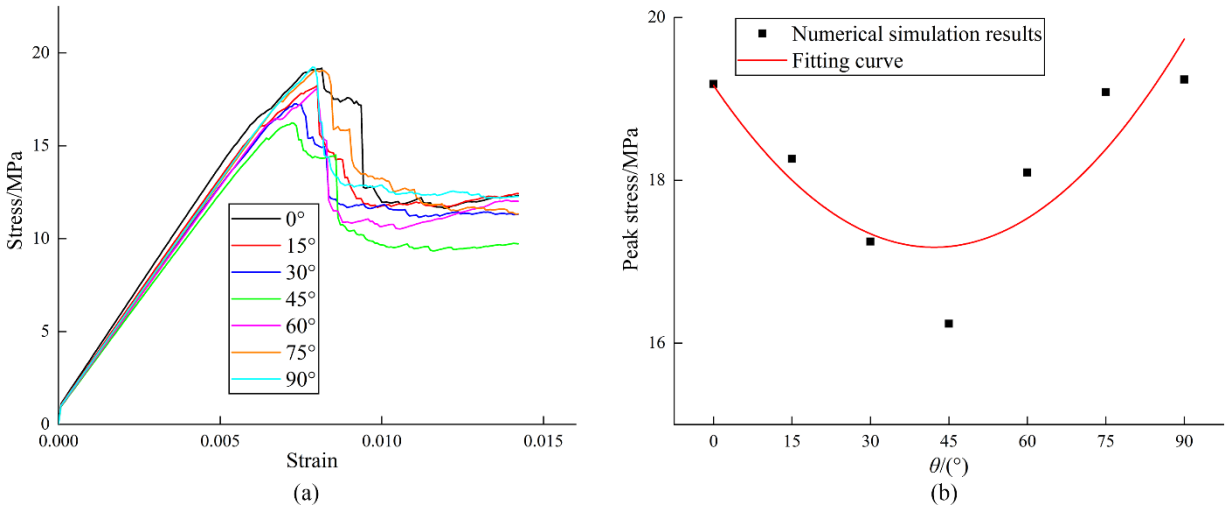

(a) Stress-strain histories (b) Peak stress

Fig. 9 Stress-strain histories and peak stress of numerical results under static loads

3. Numerical simulation

3.1 Principle of rock failure process analysis (RFPA)

To supplement the experimental results under static loads, RFPA software was applied for the numerical simulations. The numerical RFPA software has been widely applied in numerical simulations by many scholars (Li *et al.* 2019c, Liao *et al.* 2019, Tang *et al.* 2016). The simulation models are meshed using quadrilateral elements with the same dimensions, and the physical properties of all elements are statistically distributed based on a Weibull function (Xu *et al.* 2015), as follows

$$f(u)=\frac{m}{u_0}(\frac{u}{u_0})^{m-1}\exp[-(\frac{u}{u_0})^m] \tag{3}$$

In the above, u represents the element property (elastic modulus or strength); u_0 represents the average element property; m represents the shape of the Weibull function, and is denoted as the "heterogeneity index."

In this research, the maximum tensile stress criterion and Mohr–Coulomb criterion were adopted to describe the failure behaviors of the rock materials. These two criteria indicate that when the maximum tensile stress value or shear stress value of an element exceeds the corresponding limit, the element fails. The two criteria can be expressed as follows (Wang *et al.* 2016a)

$$\sigma_1 \le \sigma_t \tag{4}$$

$$\sigma_1=\frac{1+\sin\varphi}{1-\sin\varphi}\cdot\sigma_3+\frac{2C}{1-\sin\varphi} \tag{5}$$

Here, σ_1 represents the maximum principal stress; σ_3 represents the minimum principal stress; σ_t represents the tensile strength of the element; φ represents the internal friction angle; C represents the cohesion.

3.2 Simulation results under static loads

Fig. 9 shows the stress–strain histories and failure peak stress of the flawed roadway tunnel models in the numerical simulation. The stress–strain curves coincide with the experimental results under static loads (Fig. 4), indicating that the flawed roadway tunnel models show significant brittleness. The peak stress values of the flawed roadway tunnel models versus the inclination angle θ are presented in Fig. 9(b); at $\theta = 45°$, the failure peak stress is 16.24 MPa, and the strain is 0.00721, the lowest in all groups. With an increasing inclination angle θ, the failure peak stress value of each group initially decreases, and then increases. At the peak stress of $\theta = 45°$, the error with the experimental results is 8.41%. All of the peak stresses of the numerical results were listed in Table 2. The maximum error is 17.08% for $\theta = 60°$, indicating that the reduction in the compressive strength for the flawed roadway tunnel models agrees well with the predictions from the numerical simulation.

Fig. 10 illustrates the stress-strain plots and associated acoustic emission (AE) counts in the rock around the flawed roadway. As shown in Fig. 10, the failure peak stress of the flawed roadway tunnel models increases gradually and then decreases as the inclination angle θ increases from 0° to 90°. Similarly, the strain at the failure peak stress decreases and then increases as the inclination angle θ increases from 0° to 90°. In addition, the stress-strain plot and AE counts of a no-flaw tunnel roadway are also shown in Fig. 10(a); one can find that the failure stress is 19.80 MPa and the strain is 0.00821, i.e., larger than those of the other flawed roadway tunnel models. The numerical results indicate that, even in the low-dip and high-dip flawed models, the failure behaviors and strength of the model are affected by the inclination angle of the crack in the roadway.

Fig. 11 presents the fracture modes of the flawed roadway tunnel models with different inclination angles θ in the experiments and numerical simulations. It can be seen that the damages occur at the crack tip and left sidewall at θ = 0°, 15°, 30°, 45°, and 60°. Additionally, some tensile

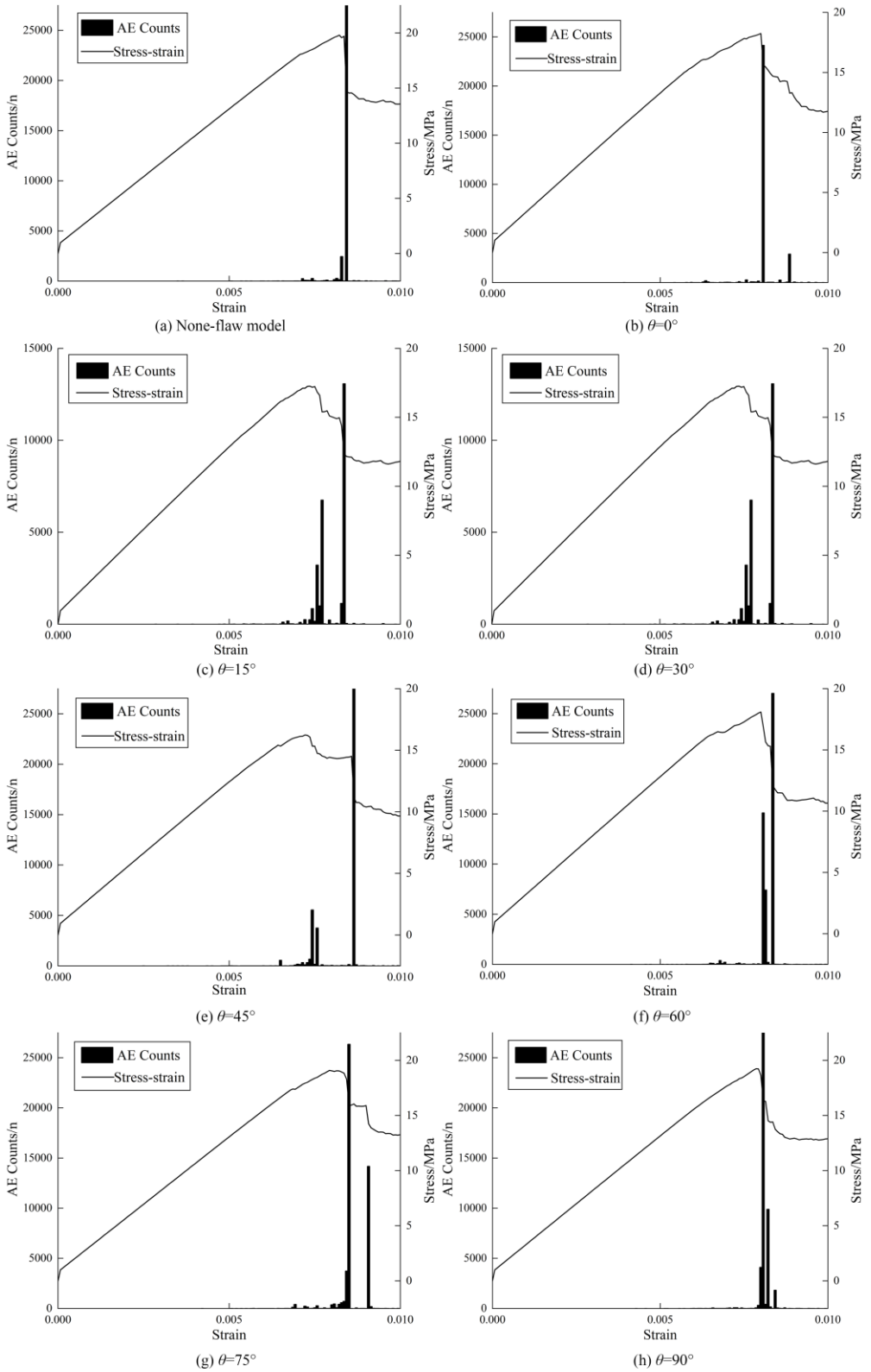

Fig. 10 Stress-strain plots and associated acoustic emission (AE) counts

cracks are produced at the bottom of the roadway tunnel models, and begin to extend along the vertical direction parallel to the direction of static loads. In the cases of θ = 75° and 90°, the damages occur at crack tip and both sides of the sidewall. Especially, at θ = 90°, the damage is symmetrical in the numerical results.

3.3 Principle of AUTODYN

Because both the deformation and the pressure in this experiment are not very large under dynamic loads, a linear EOS is implemented for the rock material. The linear EOS can be described as follows

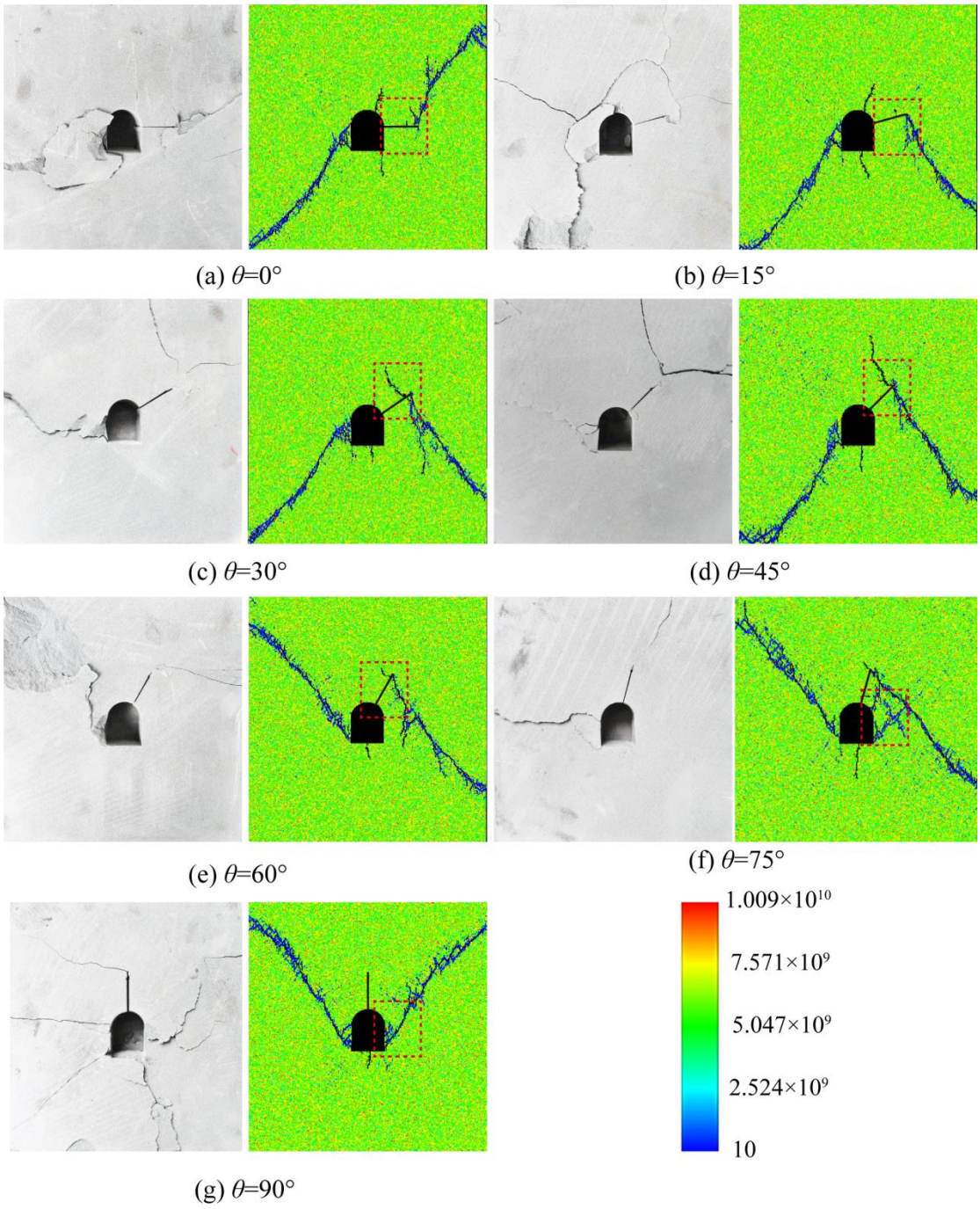

Fig. 11 Comparisons of cracking patterns between experimental results and simulation results

$$P(\rho)=\kappa\left(\frac{\rho}{\rho_0}-1\right) \tag{6}$$

In the above, κ represents the bulk modulus; ρ_0 and ρ represent the densities in the initial and current state, respectively.

Similarly, to describe the failure behaviors of rock materials under dynamic loads, the principal stress failure criteria and maximum shear stress failure criteria were adopted in the simulation models. They can be expressed as follows

$$\begin{gathered}\sigma_1 \geq \sigma_T \\ \tau_{\max}=\frac{\sigma_1-\sigma_3}{2} \geq \tau_c\end{gathered} \tag{7}$$

Here, σ_1 and σ_3 represent the maximum and minimum principal stresses, respectively; τ_{max} represents the maximum shear stress; σ_T and τ_c represent the material dynamic tensile strength and dynamic shear strength, respectively.

The rectangular elements were applied to meshing

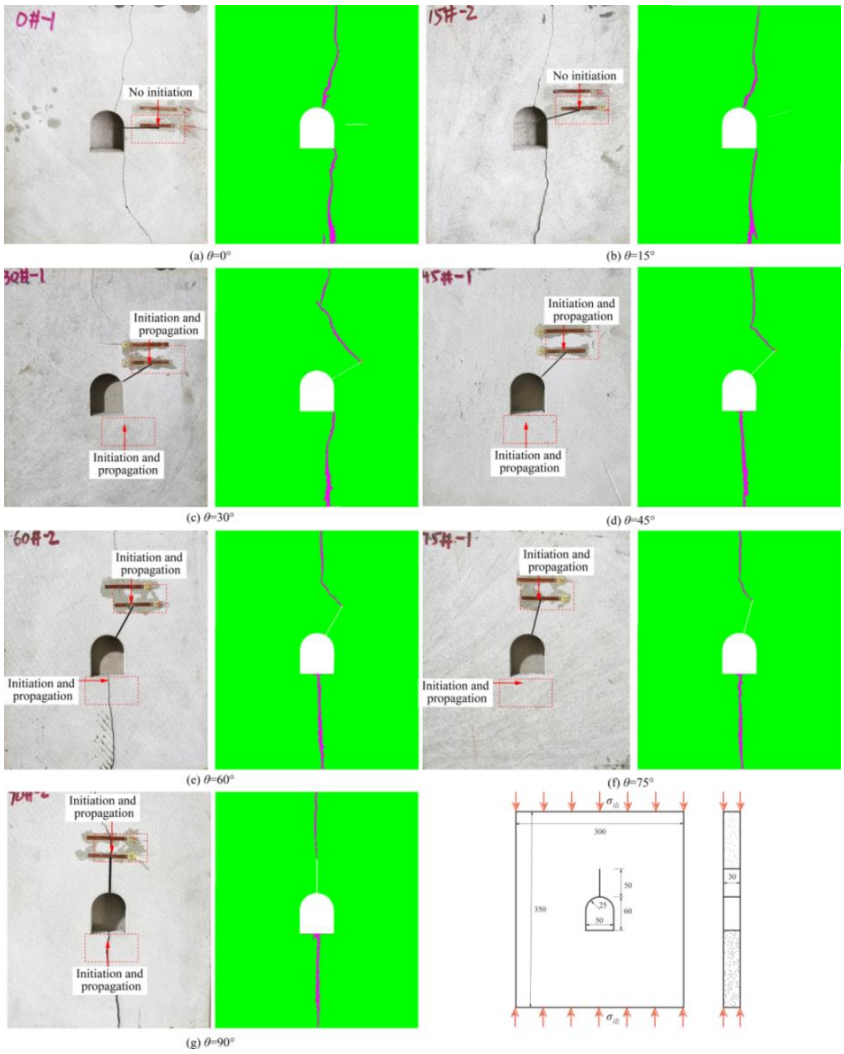

Fig. 12 Comparison of cracking patterns between test results and simulation results under dynamic loads

the incident plate, transmission plate, flawed roadway specimen, and concrete amortisseur. The total number of elements was 424353. The physical and mechanical properties of the sandstone used in the numerical simulation were presented in Table 1.

3.4 Simulation results under dynamic loads

Fig. 12 shows comparisons between the results from the numerical simulations and dynamic experiments. As shown in Fig. 12, when θ = 0° and 15°, the flaw had not initiated. However, flaws in the roadway roof and roadway foot were initiated and propagated based on forming new cracks, and most of the crack paths were on the right side of the specimen. At θ = 30°, the crack started to initiate, and the flaw in the roadway foot was initiated and propagated. As θ increased from 45° to 90°, the crack also initiated and propagated along the direction of the maximum principal stress area, and a new crack formed in the middle area of the roadway bottom, which was different from the case for θ = 0°–30°. From the failure modes of different angles θ under impact loads, one can find that the crack can guide the failure modes of the flawed roadway tunnel models.

To reveal the reasons for the crack deflections and initiation mechanisms of the flawed roadway tunnel models under impact loads, a series of gauge points were arranged in the crack tip area and inside the specimen, as shown in Fig. 13. It can be observed that the flaw initiates at 465.61 μs for θ = 90°; for θ = 30°, 45°, 60°, and 75°, the flaw initiation times are 373.73 μs, 356.16 μs, 364.75 μs, and 399.53 μs, respectively. All of these values are smaller than those from the dynamic experimental results, owing to the homogeneity assumption for the sandstone material in the numerical simulation. The errors of each group specimens were listed in Table 3 and one can find that the results of numerical simulation were agreed with the results of experimental results.

As cracks do not initiate at θ = 0° and 15°, the internal stress state of the specimen with θ = 15° was analyzed, as illustrated in Fig. 14. As can be seen, the stress σ_1 in the right part of the flawed roadway specimen is larger than that in the left part in the same specimen. The peak stress σ_1 of gauge #4 is 1.27 MPa, the peak stress σ_1 of gauge #5 is 23.57 MPa, and the peak stress σ_1 of gauge #6 is 5.82 MPa. We can see from that gauge #5 reaches the peak stress the

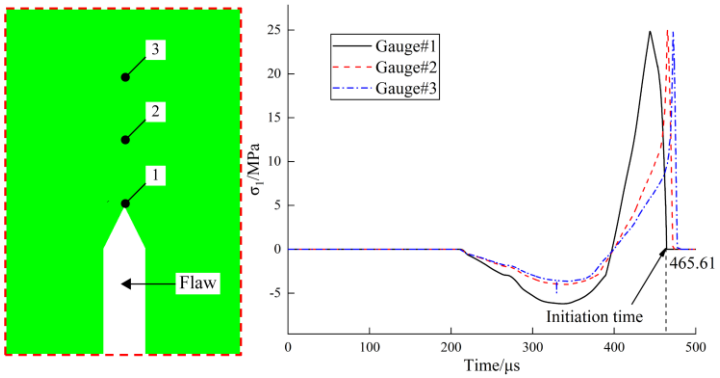

Fig. 13 Plots of maximum principal stress σ_1 for $\theta = 90°$

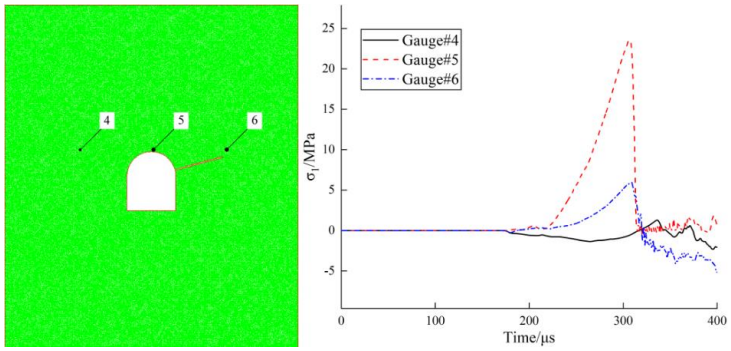

Fig. 14 Maximum principal stress σ_1 distribution of the specimen with $\theta = 15°$

earliest, and gauge #4 reaches it the latest. It can be concluded that the stress coefficient on the right side of the specimen is larger than that on the left side. The maximum principal stress in the middle area is the largest; this is why the crack propagation path is inclined to the middle area of the roadway roof.

In order to evaluate crack initiation angle under dynamic loads, the maximum circumferential stress curves were also calculated at crack initiation stage, as shown in Fig. 15. It can be seen that when the crack inclination angle θ is 90°, the crack performs a pure mode I crack initiation.

3.5 Calculation of stress intensity factor (SIF)

Crack initiation and propagation are some of the most important failure behaviors in flawed roadway tunnel models. The calculation of SIF around the crack tip is essential. To deeply understand the effects of cracks and the crack inclination angle θ on the roadway tunnel model's stability, K_I and K_{II} were calculated under static and dynamic loads by using ABAQUS software. Simulation models were built according to the dimensions illustrated in Fig. 3. The quadrilateral element CPS8 was used for the meshes, and the region around the crack tip where triangular elements CPS6 were used for describing the crack tip singularity, where $r_{OB} = 4r_{OA}$, as illustrated in Fig. 16. The flawed roadway tunnel model ($\theta = 45°$) comprised of 8386 elements and 25544 nodes.

3.5.1 Static stress intensity factor

According to the configuration of the flawed roadway tunnel models, seven numerical models were established, and the calculation results are plotted in Fig. 17. One can find that the K_I value of each group is less than zero, as the radical cracks are in compression under static loads, and will not result in a stress concentration at the crack tip. However, the static loads will cause compressive stress at the crack tip, which has an effect on the stress field. Hence, a negative K_I value will affect the crack initiation and propagation under static loads, but its influencing mechanism is not clear (Zhu *et al.* 2007, 1997). K_{II} versus the crack inclination angle θ depicted in Fig. 17. At $\theta = 45°$, the absolute value of K_{II} is at the maximum, indicating that the stress concentration coefficient at the crack tip is the largest, and that this crack is the easiest to initiate. At $\theta = 90°$, the absolute value of K_{II} is at the minimum (near 0), indicating that the flaw is a pure mode I crack. With an increase in the inclination angle θ, K_{II} initially decreases and then increases, and the numerical calculation results agree with the tendency of the compressive strength under static loads

3.5.2 Dynamic stress intensity factor

When the failure behavior of the flawed roadway tunnel models under impact loads was mainly crack initiation and propagation along the direction of the dynamic loads, indicating that the stress field analysis of the crack tip plays a particularly important role in stability assessment, the dynamic SIF (DSIF) at the crack tip was calculated. The DSIF was calculated by using ABAQUS, which has been used to evaluate the stability of rock masses by many scholars (Fan *et al.* 2017, Zhou *et al.* 2018a, Zhu *et al.* 2015).

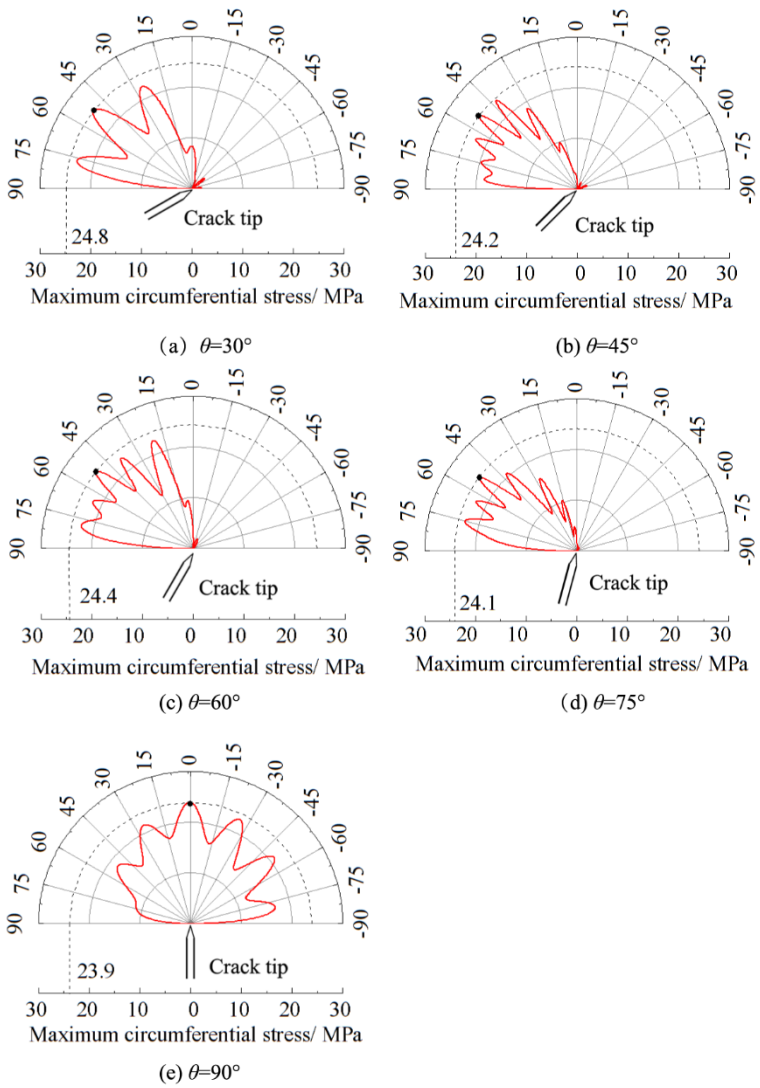

Fig. 15 Maximum circumferential stress curves of each group of specimens

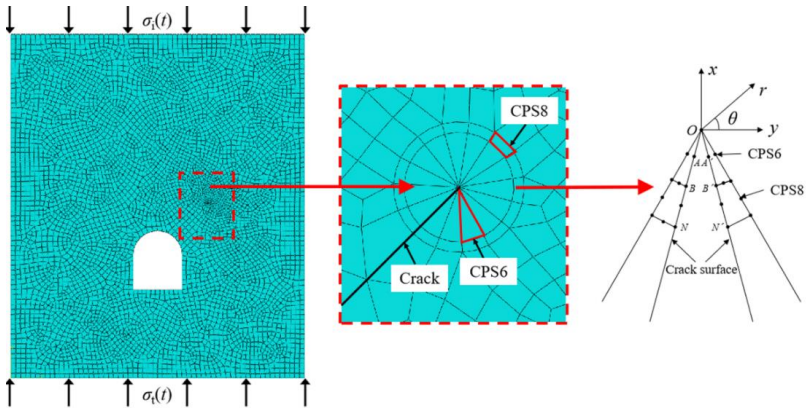

Fig. 16 Finite element model in ABAQUS

The impact loads $\sigma_i(t)$ and $\sigma_t(t)$ as calculated using Eqs. (1) and (2) were applied to both ends of the flawed models. According to the time-history curves of the DSIF and time of crack fracture initiation, the critical DSIFs in the flawed roadway tunnel models can be obtained, and the dynamic stability of the flawed roadway tunnel models can beevaluated. This approach to determining the critical DSIFs is denoted as an "experimental-numerical" approach. This approach has been widely used by scholars in recent years (Dai *et al.* 2010, Grégoire *et al.* 2009, Wang *et al.* 2016b).

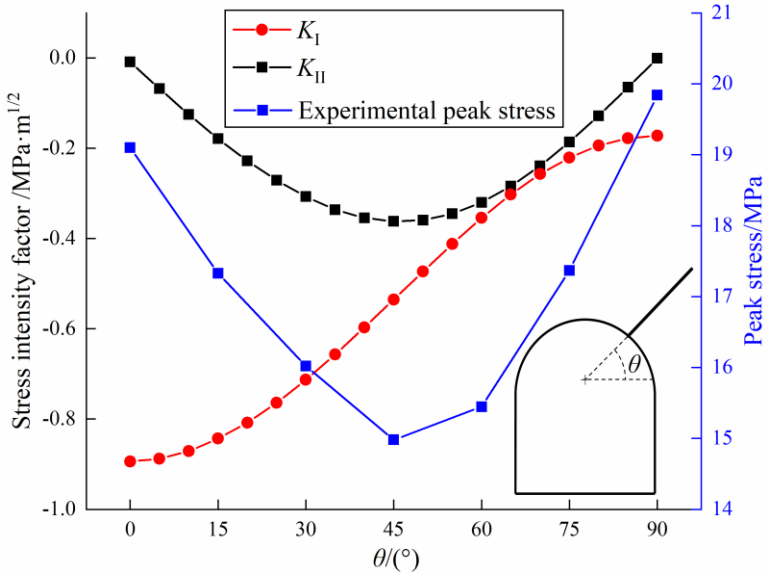

Fig. 17 Calculation results of stress intensity factors (SIFs) K_I and K_{II}

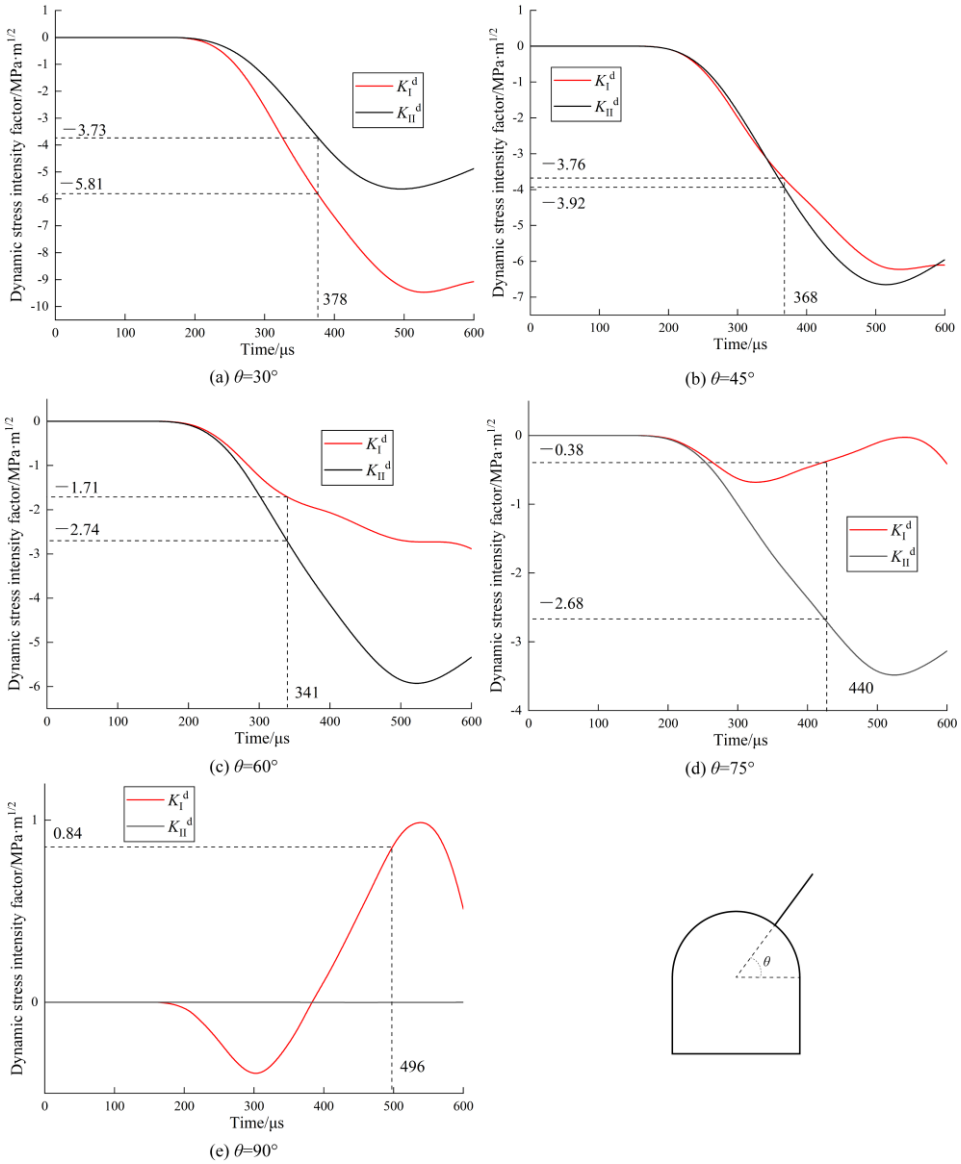

Fig. 18 Plots of DSIFs with various inclination angles θ

Fig. 18 illustrates the calculation results for the DSIF with different inclination angles θ. When θ = 90°, the corresponding crack is a pure mode I crack, and only the mode I DSIF ($K_{\mathrm{I}}^{\mathrm{d}}$) exists. However, when θ increases from 30° to 75°, modes I $K_{\mathrm{I}}^{\mathrm{d}}$ and II $K_{\mathrm{II}}^{\mathrm{d}}$ exist simultaneously, as illustrated in Figs. 18(a)-18(d); their absolute values decrease with the inclination angle θ.

Fig. 18(a) illustrates that when θ = 30°, the crack is a mixed-mode I/II crack. According to the experimental results for this specimen, the dynamic fracture initiation time is 378 μs, indicating that the mode I SIF $K_{\mathrm{I}}^{\mathrm{d}}$ = –5.81 MPa·m$^{1/2}$, and that the mode II SIF $K_{\mathrm{II}}^{\mathrm{d}}$ = –3.73 MPa·m$^{1/2}$. Similarly, for θ = 45°, 60°, and 75°, the critical values of $K_{\mathrm{I}}^{\mathrm{d}}$ =–3.76 MPa·m$^{1/2}$, −1.71 MPa·m$^{1/2}$, and −0.38 MPa·m$^{1/2}$, respectively, and those of $K_{\mathrm{II}}^{\mathrm{d}}$ = −3.92 MPa·m$^{1/2}$, −2.74 MPa·m$^{1/2}$, and −2.68 MPa·m$^{1/2}$, respectively, as illustrated in Figs. 18(b)-18(d). In addition, for the case of θ = 90°, $K_{\mathrm{II}}^{\mathrm{d}}$ is small and can be considered as negligible, as shown in Fig. 18(a). According to the experimental results for this specimen under impact loads, the dynamic fracture initiation time is 496 μs, and the corresponding critical DSIF $K_{\mathrm{I}}^{\mathrm{d}}$ =0.84 MPa·m$^{1/2}$ and $K_{\mathrm{II}}^{\mathrm{d}}$ =0 MPa·m$^{1/2}$. It is observed that the crack initiation is only related to mode I $K_{\mathrm{I}}^{\mathrm{d}}$. The calculation results of each group were listed in Table 3. One can generally conclude that the absolute values of $K_{\mathrm{I}}^{\mathrm{d}}$ and $K_{\mathrm{II}}^{\mathrm{d}}$ decrease with the inclination angle θ; this is different from the calculation results for the SIF under static loads (as shown in Fig. 4(b)). From the calculation results for the DSIF, it can be observed that the stress concentration factor at θ = 45° is the maximum for all groups, indicating that the dynamic stability of θ = 45° is minimal. Thus, the DSIF can be used to estimate the dynamic stability of flawed roadway tunnel models under dynamic loads.

4. Conclusions

In this study, numerical simulations and laboratory experiments were conducted to study the effects of different inclination angles of cracks on the stability of roadway tunnel models. The failure behaviors and stability of the flawed roadway tunnel models were evaluated under static and dynamic loads, and the failure processes were simulated by using RFPA and AUTODYN software. The dynamic stress intensity factor was calculated by using ABAQUS software. Through the comparisons in this study, some salient conclusions can be stated, as follows.

- Both cracks and the inclination angle θ have significant impacts on the stability of a roadway in a fractured rock mass. When θ = 45°, the peak stress of the flawed roadway tunnel model under static loads is 82.02% of that of an intact roadway tunnel model. This means that at θ=45°, the static stability of the flawed roadway tunnel model is the lowest.
- A mixed-mode I/II crack in the flawed roadway tunnel models subjected to static loads is likely to produce a wing crack and anti-wing crack, and the sidewalls are also damaged during the failure process. However, only a wing crack is produced at the crack tip under dynamic loads. Meanwhile, some tensile cracks are formed at the bottom of the roadway tunnel model. The stress value in the crack region is greater than that in the non-crack region, and the stress value in the middle region of the specimen is the largest; this is why the crack propagates along the maximum principal stress region.
- The fracture modes of the flawed roadway tunnel models under impact loads were mainly crack initiation and propagation, indicating that the stability of the flawed roadway tunnel models under dynamic loads is closely related to the stress field at the crack tip. As the inclination angle θ = 45°, the dynamic stability of the flawed roadway tunnel models is the lowest.

Acknowledgements

This work was financially supported by the open fund of Shock and Vibration of Engineering Materials and Structures Key Laboratory of Sichuan Province (20kfgk01); the Sichuan Science and Technology Program(2021YJ0511); the State Key Laboratory for Geo-Mechanics and Deep Underground Engineering, China University of Mining &Technology (SKLGDUEK2111); the Key Laboratory of Rock Mechanics and Geohazards of Zhejiang Province (ZJRMG-2020-01); the Major research and development project of Metallurgical Corporation of China LTD. in the non-steel field (2021-05); the Fundamental Research Funds for the Central Universities(2021SCU12130); the Sichuan University postdoctoral interdisciplinary Innovation Fund.

References

Ajdani, A., Ayatollahi, M.R., Akhavan-Safar, A. and Martins da Silva, L.F. (2020), “Mixed mode fracture characterization of brittle and semi-brittle adhesives using the SCB specimen”, *Int. J. Adhes. Adhes.*, **101**, 102629. https://doi.org/10.1016/j.ijadhadh.2020.102629.

Aliha, M.R.M. and Ayatollahi, M.R. (2014), “Rock fracture toughness study using cracked chevron notched Brazilian disc specimen under pure modes I and II loading – A statistical approach”, *Theor. Appl. Fract. Mech.*, **69**, 17-25. https://doi.org/10.1016/j.tafmec.2013.11.008.

Aliha, M.R.M., Bahmani, A. and Akhondi, Sh. (2016), “Mixed mode fracture toughness testing of PMMA with different three-point bend type specimens”, *Eur. J. Mech. –A Solids* **58**, 148-162. https://doi.org/10.1016/j.euromechsol.2016.01.012.

Alneasan, M., Behnia, M. and Bagherpour, R. (2019), “Analytical and numerical investigations of dynamic crack propagation in brittle rocks under mixed mode loading”, *Constr. Build. Mater.*, **222**, 544-555. https://doi.org/10.1016/j.conbuildmat.2019.06.163.

Dai, F., Chen, R., Iqbal, M.J. and Xia, K. (2010), “Dynamic cracked chevron notched Brazilian disc method for measuring rock fracture parameters”, *Int. J. Rock Mech. Min. Sci.*, **47**(4), 606-613. https://doi.org/10.1016/j.ijrmms.2010.04.002.

Du, S., Li, D., Yu, W., Zhang, J. and Liu, F. (2020), "Stability Analysis and Support Control for a Jointed Soft Rock Roadway Considering Different Lateral Stresses", *Geotech. Geol. Eng.*, **38**(1), 237-253. https://doi.org/10.1007/s10706-019-01013-w.

Fan, Y., Zhao, Y., Zhu, Z., Zhou, L. and Dong, Y. (2017), "Stress intensity factors for a tunnel containing a radial crack under compression", *Adv. Mech. Eng.*, **9**(12), 168781401774541. https://doi.org/10.1177/1687814017745414.

Fan, Y., Zhu, Z., Zhao, Y., Zhou, C. and Zhang, X. (2019), "The effects of some parameters on perforation tip initiation pressures in hydraulic fracturing", *J. Pet. Sci. Eng*., **176**, 1053-1060. https://doi.org/10.1016/j.petrol.2019.02.028.

Grégoire, D., Maigre, H. and Combescure, A. (2009), "New experimental and numerical techniques to study the arrest and the restart of a crack under impact in transparent materials", *Int. J. Solids Struct.*, **46**(18-19), 3480-3491. https://doi.org/10.1016/j.ijsolstr.2009.06.003.

Haeri, H., Sarfarazi, V., Bagher Shemirani, A. and Fatehi Marji, M. (2018), "On the direct experimental measurement of mortar fracture toughness by a compression-to-tensile load transformer (CTLT)", *Constr. Build. Mater*., **181**, 687-712. https://doi.org/10.1016/j.conbuildmat.2018.06.066.

Haeri, H., Sarfarazi, V., Ebneabbasi, P., Nazari maram, A., Shahbazian, A., Fatehi Marji, M. and Mohamadi, A.R. (2020), "XFEM and experimental simulation of failure mechanism of non-persistent joints in mortar under compression", *Constr. Build. Mater*., **236**, 117500. https://doi.org/10.1016/j.conbuildmat.2019.117500.

Haeri, H., Shahriar, K., Marji, M.F. and Moarefvand, P. (2014), "Cracks coalescence mechanism and cracks propagation paths in rock-like specimens containing pre-existing random cracks under compression", *J. Cent. South Univ*., **21**(6), 2404-2414. https://doi.org/10.1007/s11771-014-2194-y.

Huang, X., Tang, S.B., Tang, C.A., Xie, L.M. and Tao, Z.Y. (2017), "Numerical simulation of cracking behavior in artificially designed rock models subjected to heating from a central borehole", *Int. J. Rock Mech. Min. Sci.*, **98**, 191-202. https://doi.org/10.1016/j.ijrmms.2017.07.016.

Huang, Y.H., Yang, S.Q. and Tian, W.L. (2019), "Crack coalescence behavior of sandstone specimen containing two pre-existing flaws under different confining pressures", *Theor. Appl. Fract. Mech.*, **99**, 118-130. https://doi.org/10.1016/j.tafmec.2018.11.013.

Jia, P. and Tang, C.A. (2008), "Numerical study on failure mechanism of tunnel in jointed rock mass", *Tunn. Undergr. Sp. Tech*., **23**(5), 500-507. https://doi.org/10.1016/j.tust.2007.09.001.

Lesiuk, G., Smolnicki, M., Mech, R., Zięty, A. and Fragassa, C. (2020), "Analysis of fatigue crack growth under mixed mode (I + II) loading conditions in rail steel using CTS specimen", *Eng. Fail. Anal.*, **109**, 104354. https://doi.org/10.1016/j.engfailanal.2019.104354.

Li, D., Han, Z., Sun, X., Zhou, T. and Li, X. (2019a), "Dynamic mechanical properties and fracturing behavior of marble specimens containing single and double flaws in SHPB tests", *Rock Mech. Rock Eng.*, **52**(6), 1623-1643. https://doi.org/10.1007/s00603-018-1652-5.

Li, D., Han, Z., Zhu, Q., Zhang, Y. and Ranjith, P.G. (2019b), "Stress wave propagation and dynamic behavior of red sandstone with single bonded planar joint at various angles", *Int. J. Rock Mech. Min*., **117**, 162-170. https://doi.org/10.1016/j.ijrmms.2019.03.011.

Li, G., Cheng, X.F., Pu, H. and Tang, C.A. (2019c), "Damage smear method for rock failure process analysis", *J. Rock Mech. Geotech. Eng*., **11**(6), 1151-1165. https://doi.org/10.1016/j.jrmge.2019.06.007.

Li, M., Zhu, Z., Liu, R., Liu, B., Zhou, L. and Dong, Y. (2018), "Study of the effect of empty holes on propagating cracks under blasting loads", *Int. J. Rock Mech. Min*., **103**, 186-194. https://doi.org/10.1016/j.ijrmms.2018.01.043.

Liao, Z.Y., Zhu, J.B. and Tang, C.A. (2019) "Numerical investigation of rock tensile strength determined by direct tension, Brazilian and three-point bending tests", *Int. J. Rock Mech. Min*., **115**, 21-32. https://doi.org/10.1016/j.ijrmms.2019.01.007.

Mitra, E., Hazell, P.J. and Ashraf, M. (2015), "A discrete element model to predict the pressure-density relationship of blocky and angular ceramic particles under uniaxial compression", *J. Mater. Sci*., https://doi.org/10.1007/s10853-015-9344-y.

Reddish, D.J., Stace, L.R., Vanichkobchinda, P. and Whittles, D.N. (2005), "Numerical simulation of the dynamic impact breakage testing of rock", *Int. J. Rock Mech. Min.*, **42**(2), 167-176. https://doi.org/10.1016/j.ijrmms.2004.06.004.

Rege, K., Grnsund, J. and Pavlou, D.G. (2019), "Mixed-mode I and II fatigue crack growth retardation due to overload: An experimental study", *Int. J. Fatigue*, **129**, 105227. https://doi.org/10.1016/j.ijfatigue.2019.105227.

Sarfarazi, V., Haeri, H. and Fatehi, M. (2017), "Fracture Mechanism of Brazilian Discs with Multiple Parallel Notches Using PFC2D", *Period. Polytech. Civ. Eng.*, https://doi.org/10.3311/PPci.10310.

Sarfarazi, V., Haeri, H., Ebneabbasi, P., Shemirani, A.B. and Hedayat, A. (2018), "Determination of tensile strength of concrete using a novel apparatus", *Constr. Build. Mater*., **166**, 817-832. https://doi.org/10.1016/j.conbuildmat.2018.01.157.

Shi, G.H. 1992 "Discontinuous Deformation Analysis: A New Numerical Model for the Statics and Dynamics of Deformable Block Structures". *Eng. Comput.*, https://doi.org/10.1108/eb023855.

Tang, C., Tang, S., Gong, B. and Bai, H. (2015), "Discontinuous deformation and displacement analysis: From continuous to discontinuous", *Sci. China-Technol. Sci.*, **58**(9), 1567-1574. https://doi.org/10.1007/s11431-015-5899-8.

Tang, S.B., Zhang, H., Tang, C.A. and Liu, H.Y. (2016), "Numerical model for the cracking behavior of heterogeneous brittle solids subjected to thermal shock", *Int. J. Solids Struct*., **80**, 520-531. https://doi.org/10.1016/j.ijsolstr.2015.10.012.

Wang, L., Zhu, Z., Zhou, L., Gao, W., Dong, Y., Niu, C. and Ai, T. (2021), "Study the effect of circular hole on dynamic fracture properties of cracked PMMA specimen under impact loads", *Int. J. Impact Eng*., **156**, 103948. https://doi.org/10.1016/j.ijimpeng.2021.103948.

Wang, M., Zhu, Z., Dong, Y. and Zhou, L. (2017), "Study of mixed-mode I/II fractures using single cleavage semicircle compression specimens under impacting loads", *Eng. Fract. Mech.*, **177**, 33-44. https://doi.org/10.1016/j.engfracmech.2017.03.042.

Wang, Q., Zhu, W., Xu, T., Niu, L. and Wei, J. (2016a), "Numerical Simulation of Rock Creep Behavior with a Damage-Based Constitutive Law", *Int. J. Geomech.*, **17**, 04016044. https://doi.org/10.1061/(ASCE)GM.1943-5622.0000707.

Wang, Q.Z., Feng, F., Ni, M. and Gou, X.P. (2011), "Measurement of mode I and mode II rock dynamic fracture toughness with cracked straight through flattened Brazilian disc impacted by split Hopkinson pressure bar", *Eng. Fract. Mech*., **78**(12), 2455-2469. https://doi.org/10.1016/j.engfracmech.2011.06.004.

Wang, Q.Z., Yang, J.R., Zhang, C.G., Zhou, Y., Li, L., Wu, L.Z. and Huang, R.Q. (2016b), "Determination of dynamic crack initiation and propagation toughness of a rock using a hybrid experimental-numerical approach", *J. Eng. Mech.*, **142**(12), 1-9. https://doi.org/10.1061/(ASCE)EM.1943-7889.0001155.

Wu, F., Gao, R., Zou, Q., Chen, J., Liu, W. and Peng, K. (2020), "Long-term strength determination and nonlinear creep damage constitutive model of salt rock based on multistage creep test:

Implications for underground natural gas storage in salt cavern", *Energy Sci. Eng*., **8**(5), 1592-1603. https://doi.org/10.1002/ese3.617.

Wu, Q., Weng, L., Zhao, Y., Guo, B. and Luo, T. (2019), "On the tensile mechanical characteristics of fine-grained granite after heating/cooling treatments with different cooling rates", *Eng. Geol.*, **253**, 94-110. https://doi.org/10.1016/j.enggeo.2019.03.014.

Xie, L.X., Yang, S.Q., Gu, J.C., Zhang, Q.B., Lu, W.B., Jing, H.W. and Wang, Z.L. (2019), "JHR constitutive model for rock under dynamic loads", *Comput. Geotech*., **108**, 161-172. https://doi.org/10.1016/j.compgeo.2018.12.024.

Xu, T., He, Z.J., Tang, C.A., Zhu, W.C. and Ranjith, P.G. (2015), "Finite element analysis of width effect in interface debonding of FRP plate bonded to concrete", *Finite Elem. Anal. Des*., **93**, 30-41. https://doi.org/10.1016/j.finel.2014.08.009.

Xu, Z. and Li, Y. (2012), "A novel method in determination of dynamic fracture toughness under mixed mode I/II impact loading", *Int. J. Solids Struct.*, **49**(2), 366-376. https://doi.org/10.1016/j.ijsolstr.2011.10.011.

Ying, P., Zhu, Z., Zhou, L., Fan, Y., Dong, Y. and Wang, M. (2020), "Testing Method of Rock Dynamic Fracture Toughness Using Large Single Cleavage Semicircle Compression Specimens", *J. Test. Eval.*, **48**(5), 20170702. https://doi.org/10.1520/JTE20170702.

Yu, L., Zhang, Z., Wu, J., Liu, R., Qin, H. and Fan, P. (2020), "Experimental study on the dynamic fracture mechanical properties of limestone after chemical corrosion", *Theor. Appl. Fract. Mech.*, **108**, 102620. https://doi.org/10.1016/j.tafmec.2020.102620.

Zhou, L., Zhu, Z., Dong, Y. and Niu, C. (2020), "Investigation of dynamic fracture properties of multi-crack tunnel samples under impact loads", *Theor. Appl. Fract. Mech.*, **109**, 102733. https://doi.org/10.1016/j.tafmec.2020.102733.

Zhou, L., Zhu, Z., Liu, B. and Fan, Y. (2018a), "The effect of radial cracks on tunnel stability", *Geomech. Eng.*, **15**(2), 721-728. https://doi.org/10.12989/gae.2018.15.2.721.

Zhou, L., Zhu, Z., Qiu, H., Zhang, X. and Lang, L. (2018b), "Study of the effect of loading rates on crack propagation velocity and rock fracture toughness using cracked tunnel specimens", *Int. J. Rock Mech. Min. Sci.*, **112**, 25-34. https://doi.org/10.1016/j.ijrmms.2018.10.011.

Zhou, Q., Zhu, Z., Wang, X., Zhou, J., Lang, L. and Zhang, X. (2019), "The effect of a pre-existing crack on a running crack in brittle material under dynamic loads", *Fatigue Fract. Eng. Mater. Struct.*, **42**(11), 2544-2557. https://doi.org/10.1111/ffe.13105.

Zhu, Z., Li, Y., Xie, J. and Liu, B. (2015), "The effect of principal stress orientation on tunnel stability", *Tunn. Undergr. Sp. Tech.,* **49**, 279-286. https://doi.org/10.1016/j.tust.2015.05.009.

Zhu, Z., Mohanty, B. and Xie, H. (2007), "Numerical investigation of blasting-induced crack initiation and propagation in rocks", *Int. J. Rock Mech. Min. Sci.*, **44**(3), 412-424. https://doi.org/10.1016/j.ijrmms.2006.09.002.

Zhu, Z., Xie, H. and Ji, S. (1997), "The mixed boundary problems for a mixed mode crack in a finite plate", *Eng. Fract. Mech.*, **56**(5), 647-655. https://doi.org/10.1016/S0013-7944(96)00123-3.

Zuo, Y., Zhang, Q., Xu, T., Liu, Z., Qiu, Y. and Zhu, W. (2015), "Numerical Tests on Failure Process of Rock Particle under Impact Loading", *Shock Vib.*, **2015**, 1-12. https://doi.org/10.1155/2015/678573.